Original Article

Electronic transport, ionic activation energy and trapping phenomena in a polymer-hybrid halide perovskite composite

Mauro Leoncini [a, b], Roberto Giannuzzi [a, b], Antonella Giuri [a], Silvia Colella [c], Andrea Listorti [a, d], Vincenzo Maiorano [a], Aurora Rizzo [a], Giuseppe Gigli [a, b], Salvatore Gambino [a, *]

[a] CNR NANOTEC — Istituto di Nanotecnologia, C/o Campus Ecotekne, Via Monteroni, 73100, Lecce, Italy
[b] Dipartimento di Matematica e Fisica "E. De Giorgi", Università Del Salento, Campus Ecotekne, Via Arnesano, 73100, Lecce, Italy
[c] CNR NANOTEC - Istituto di Nanotecnologia, C/o Dipartimento di Chimica, Università di Bari, Via Orabona 4, 70126, Bari, Italy
[d] Dipartimento di Chimica, Università di Bari, Via Orabona 4, 70126, Bari, Italy

ARTICLE INFO

ABSTRACT

The exploitation of methylammonium lead iodide perovskite-polymer composites is a promising strategy for the preparation of photoactive thin layers for solar cells. The preparation of these composites is a simple fabrication method with improved moisture stability when compared to that of pristine perovskite films. To deepen the understanding of the charge transport properties of these films, we investigated charge carrier mobility, traps, and ion migration. For this purpose, we applied a combinatory measurement approach that proves how such composites can still retain an ambipolar charge transport nature and the same mobility values of the related perovskite. Furthermore, thermally stimulated current measurements revealed that the polymer influenced the creation of additional defects during film formation without affecting charge mobility. Finally, impedance spectroscopy measurements suggested the addition of starch may hinder ion migration, which would require larger activation energies to move ions in composite films. These results pave the way for new strategies of polymer-assisted perovskite film development.

© 2021 The Authors. Publishing services by Elsevier B.V. on behalf of Vietnam National University, Hanoi. This is an open access article under the CC BY-NC-ND license (http://creativecommons.org/licenses/by-nc-nd/4.0/).

1. Introduction

Hybrid (organic-inorganic) perovskite semiconductors are currently among the most promising candidates for the development of alternative solar cells. In less than ten years, perovskite solar cells (PSCs) have reached a power conversion efficiency (PCE) of 25.5% [1]. Despite this remarkable achievement in device efficiency, which makes PSCs already suitable for the market, properties like straightforward processing and operative device stability are often below the standard to be technologically scaled up. For example, top-performing PSCs are realized by solution cast techniques like ink-jet, slot die, spray coating, or roll-to-roll methods [2], all of which require a "timely" anti-solvent dripping that is hardly suitable for large scale production.

Over the last few years, the use of polymers as templating agents for the growth of hybrid perovskite materials has emerged as an efficient strategy to confer improved stability and processability to the active layer [3—5]. In particular, our group has developed a methylammonium lead iodide (MAPbI$_3$) perovskite-starch composite (so-called MAPI-composite), which has been used as a light harvester for solar cells [3,6] and light-emitting devices [7]. These devices are characterized by a simple fabrication process and result in improved device stability while maintaining similar performance compared to that of pristine perovskite-based devices. In order to understand the limits and advantages of these composites, it is important to investigate their charge transport mechanism as it is strictly related to device efficiency. The composite we propose in this research consists of an active (perovskite) and a passive (starch) component, the latter of which has been demonstrated to be beneficial for i) the formation of perovskites via a single-step polymer-assisted anti-solvent free process, ii) film stability, and iii) mechanical stress [3]. However,

* Corresponding author.
 E-mail address: salvatore.gambino@nanotec.cnr.it (S. Gambino).
 Peer review under responsibility of Vietnam National University, Hanoi.

with the composite being an insulator, it does not play any active role in electronic charge transport. Furthermore, in a composite, defect states arising from boundaries between the perovskite and polymer may introduce traps and recombination centres that would have a direct influence on the transport mechanism of the charge carriers and thus on device efficiency. Other solution-processable materials like organic semiconductors have demonstrated that carrier mobility depends on a wide range of factors such as the materials' chemical structure, molecular weight, processing conditions (solvents, casting technique), and environmental conditions [8]. Furthermore, in perovskites, the study of the electronic charge transport mechanism is even more complex because it is also influenced by ionic conduction. Thus, mixed ionic and electronic charge transport must be considered [9—11].

To better address this challenge, we combine space charge limited current (SCLC) measurements with other methods of investigation, such as thermally stimulated current (TSC) and impedance spectroscopy (IS), to access the main parameters governing the charge transport of the proposed MAPI-composite. By combining these different techniques, we disentangle the dependence of electronic transport from ionic transport and reveal electronic (mobility and trapping phenomena) and ionic (activation energies) charge transport dynamics. We demonstrate that the MAPI-composite still retains ambipolar charge transport nature and the same mobility values of the perovskite. This is the first time that the electro-optical properties of such a MAPI-composite have been studied. Moreover, we were also able to correlate these properties to solar cells performance and film morphology.

2. Experimental

Ultra-dry 99.999 % lead (II) iodide (PbI_2) (metal basis) was purchased from Alfa Aesar; methylammonium iodide (MAI) was obtained from Greatcell Solar; corn starch (Maizena) was supplied from Sigma—Aldrich; PEDOT:Complex (PEDOT:Cx) (HTL Solar 3) was supplied from Heraeus; poly [N,N0-bis(4-butylphenyl)-N,N0-bis(phenyl) benzidine] (poly-TPD) from Solaris Chem Inc.; [6,6]-phenyl C_{61} butyric acid methyl ester (PCBM) was purchased from Nano-c. All the materials were used as received without further purification. Solution preparation and device realization are reported in the appendix.

MAPI thin films were realized via a standard one-step procedure inside an N_2 filled glove-box. First, perovskite precursors in DMF/DMSO solution were spin cast at 4000 rpm for 25 s, during which a "timely" (after 10 s) anti-solvent of 200 μl toluene was dropped on top. Subsequently, the spin-coated film was annealed onto a hot plate at 100 °C for 10 min (Fig. 1, top). Meanwhile, the MAPI-composite thin film was realized via a one-step polymer-assisted anti-solvent free procedure. The MAPI-composite solution in DMSO was spin cast at 9000 rpm for 20 s and then directly annealed on a hot plate at 100 °C for 30 min (Fig. 1, bottom).

2.1. XRD and SEM thin films characterization

X-ray diffraction (XRD) spectra of the perovskite films were acquired at room temperature by a PANanalytical X'Pert-PRO MRD diffractometer equipped with a Cu Kα source (λ = 1.5405 Å). The scanning electron microscopy (SEM) images were collected with Carl Zeiss Auriga 40 Crossbeam (Zeiss) instrument in high vacuum and high-resolution mode at 5 kV acceleration voltage and was equipped with Gemini column and an integrated high efficiency in-lens detector.

SCLC measurements were performed in the dark and the sample was loaded into a cryostat under low dynamic vacuum (10^{-2} mbar).

Current—voltage characteristics were recorded using a computer controlled pico-ammeter (HP 4140B).

TSC measurements were performed by loading the sample into a sample stage (Linkam LTS420E-P) and maintaining it under dynamic vacuum. The temperature was allowed to vary between 77 K and 300 K. Trap filling was achieved by illuminating the sample via a halogen lamp for 5 min at 160 K. After a dwell time of 15 min at 160 K without light, the temperature was increased at a constant rate of 5 K/min. Thermally stimulated currents were recorded using a computer controlled pico-ammeter (HP 4140B) without applying an external bias to the device.

Impedance spectroscopy was carried out at different temperatures by loading the sample into a sample stage (Linkam LTS420E-P) under illumination using a white LED. IS measurements were performed at short-circuit with a 20 mV perturbation in the 10^6-10^{-2} Hz range using an Autolab/PGSTAT302N (Eco-Chemie, The Netherlands) operating in two-electrode mode. NOVA 1.11 software was used to generate data. Z-view equivalent circuit modelling software (Scribner) was used to fit the spectra.

3. Results and discussion

3.1. Perovskite solar cells

Perovskite solar cells based on MAPI and MAPI-composite films were realized in a p-i-n configuration as shown in Fig. 2a (inset), which is also where the current-density-voltage (J-V) characteristics are shown. The main PSC parameters, together with statistical data (average values) estimated for more than ten devices realized and characterized under the same experimental conditions, are reported in Table 1. It is clear that MAPI and MAPI-composite based PSCs exhibit similar performances both in terms of power conversion efficiency (PCE ≈ 17—18%) as well as fill factor (FF ≈ 76—78%), short-circuit current (J_{sc} ≈ 20—21 mA/cm^2), and V_{oc} ≈ 1.1 V. The incident photon to current conversion efficiency (IPCE) spectra of both the MAPI and MAPI-composite based solar cells are shown Fig. 2b, which are consistent with both MAPI and MAPI-composite thin film absorption spectra reported in Fig. S1. The integrated photocurrent densities are 20.8 and 19.2 mA/cm^2 for PSCs with MAPI and MAPI-composite, respectively, which are in good agreement with J_{sc} determined from the J—V curves. A complete study on MAPI-composite optimization has been reported elsewhere [3].

In order to understand how the polymer influences the electronic and ionic properties of the PSCs active layer, we performed a comprehensive study including space charge limited current, thermally stimulated currents, and impedance spectroscopy measurements, respectively.

3.2. Characterization of hole- and electron-only devices by SCLC

SCLC measurements are a relatively simple and powerful method to determine charge carrier mobilities and trap density in the so-called hole-only and electron-only devices [12]. It has been widely used to study steady state charge transport properties in organic semiconductors and also in perovskites. Recently, it has been reported that the classical numerical model, characterized by low permittivity without ion dynamics, is not strictly applicable to SCLC characteristics in perovskites [9,13]. A more complex numerical model, which considers a mixed ionic and electronic conduction, definitely leads to better fit of the entire J-V characteristics and it allows a better understanding of the physical phenomena governing this new class of materials [13]. While keeping this in mind, analytical equations remain a powerful tool to fit the experimental data in a narrow range of the J-V
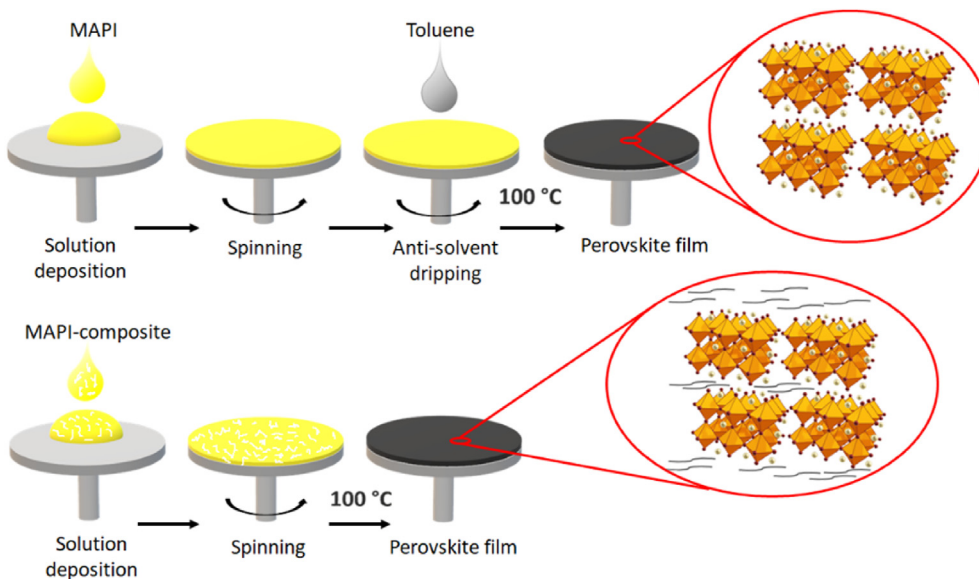
Fig. 1. Schematic illustration of the standard one-step (top) and one-step anti-solvent free (bottom) deposition methods for the synthesis of MAPI and MAPI-composite thin films.
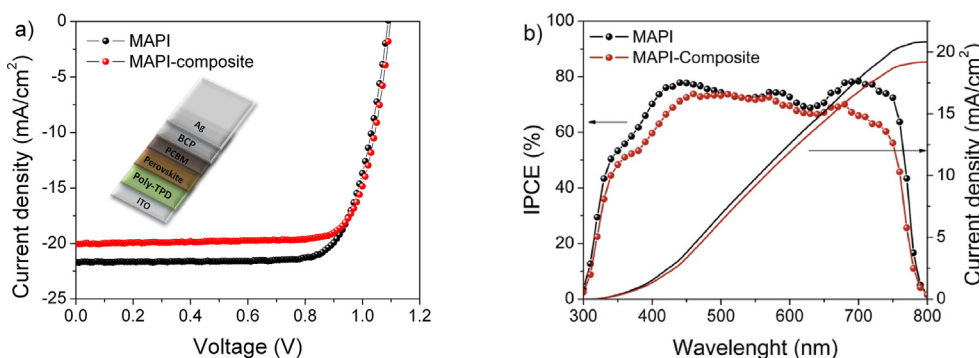

Fig. 2. Best samples of the MAPI and MAPI-composite solar cells: a) current–voltage characteristics and b) incident photon to current conversion efficiency (IPCE) spectra and the integrated current density. Schematic of the device architecture (inset).

Table 1
Solar cell parameters extracted from the best pixels for the MAPI and MAPI-composite. Average values are reported in brackets.

Perovskite	FF (%)	V_{OC} (V)	J_{SC} (mA/cm^2)	PCE (%)
MAPI	76.0 (77 ± 4)	1.09 (1.08 ± 0.02)	21.4 (20 ± 1)	17.7 (17 ± 2)
MAPI-composite	78.1 (72 ± 6)	1.10 (1.08 ± 0.02)	20.0 (19 ± 1)	17.2 (15 ± 3)

characteristics, such as the "trap-free regime", allowing us to estimate charge carriers mobility.

Hole mobility measurements were performed on unipolar devices having the following structure: ITO/PEDOT/Perovskite/MoO$_3$/Au. Fig. 3a shows a schematic of the energy levels for the hole-only devices.

In the case of MAPI-based devices, we clearly identify four regimes (see Fig. 4a) with each one characterized by a different power-low voltage dependence on the current ($J \propto V^n$). At low voltages, the current is proportional to the applied bias in the so-called ohmic regime (n = 1), which reflects the presence of good ohmic contacts and where the current derives from the equilibrium charges. As the external bias is increased, we enter into the so-called space charge regime where the injected charge density exceeds the intrinsic free carrier density and the current is bulk limited. We identify three space charge limited current regimes: i) trap-limited SCLC (TL-SCLC),

where the current is proportional to the square of the applied voltage (n = 2) typical of a "pure" space charge regime (however, its amplitude is much lower due to the presence of traps which limit the current flow); ii) as we increase the external bias further, the density of free carriers starts to exceed the trapped ones and we have the so-called trap-filling regime (TFL-SCLC, n > 3); iii) finally, once all the traps have been filled, all the injected charges participate in the current flow and give rise to trap-free charge transport (TF-SCLC) where the current–voltage characteristic is described by the well-known Mott–Gurney relation (n = 2) [14]:

$$J = \frac{9}{8}\mu\varepsilon_r\varepsilon_0\frac{V^2}{L^3} \tag{1}$$

where V is the external applied voltage, μ is the "trap-free" mobility, ε_0 the vacuum permittivity, ε_r the relative permittivity,
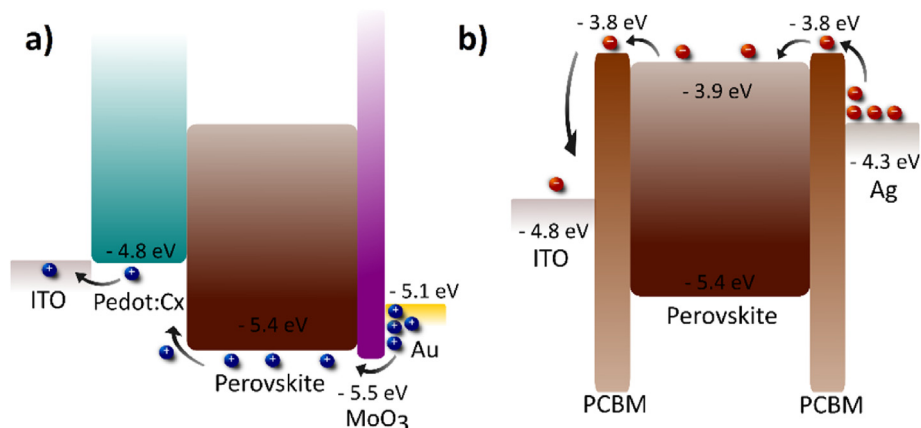
Fig. 3. Schematic of the energy levels of the (a) hole-only and (b) electron-only devices realized for the SCLC measurements.
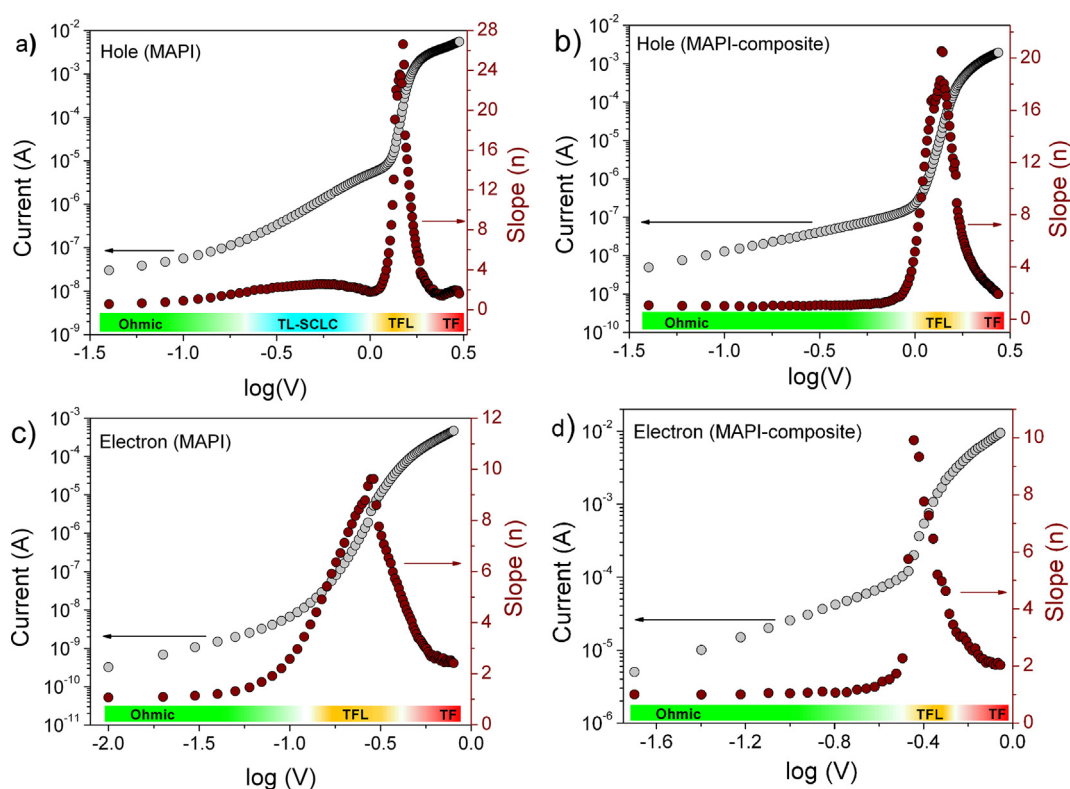

Fig. 4. Current- and slope−voltage curves for the hole-only and electron-only devices for the (a,c) MAPI and the (b,d) MAPI-composite.

and L is the sample thickness. This latter regime allowed us to determine the mobility values by fitting the current−voltage characteristics according to Eq. (1) (see Fig. S5). The average hole mobility, estimated from several nominal identical devices, was found to be $(1.1 \pm 0.3) \times 10^{-3}$ cm^2/Vs for MAPI, which is in good agreement with previously reported results [15,16]. In similar way, we measured the average hole mobility of the MAPI-composite and it was found to be $(1.8 \pm 0.8) \times 10^{-3}$ cm^2/Vs. We can clearly see that as we move from a neat perovskite active layer to a MAPI-composite, the charge carrier mobility does not change. This result implies a good optimization of the perovskite-polymer ratio [3], which allows a percolation path between the perovskite sites that gives a hole mobility similar to that of the pristine film. This latter observation can explain the similar performances of

MAPI and MAPI-composite solar cells (see Table 1). Furthermore, from the analysis of the current−voltage curves, the TL-SCLC regime is missing in the MAPI-composite sample, which shows a direct transition from the ohmic to the TFL regime. The presence of a broad peak in the slope, between the linear regime and the TFL one, can be ascribed to trap sites [17,18]. We argue that the polymer could inhibit the formation of these trap sites close to the valence band. The suppression of these traps can occur either during film processing or by hindering the drift of positive ions, leaving fixed negatively-charged ions, which may act as trap states for positive free carriers (holes) [19−21]. Usually, the TFL regime allows the quantification of the trap density via the so-called V_{TFL}, which is based on a simplified model that assumes a single level of traps [14,22]. In the present case, anticipating later
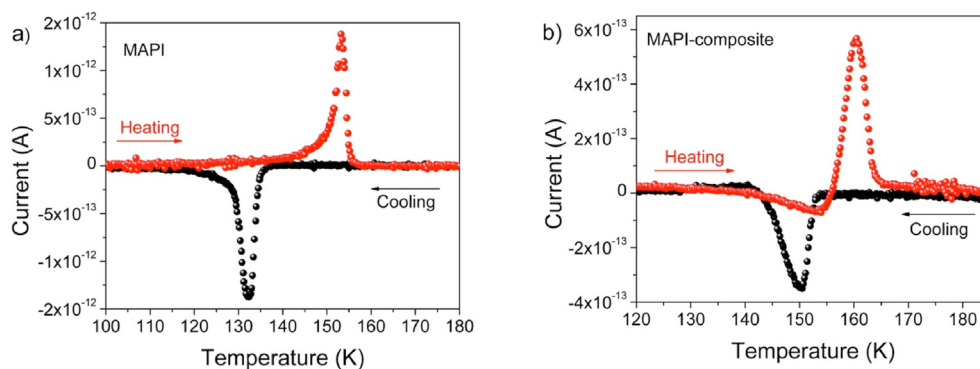
Fig. 5. Phase transition for the (a) MAPI and (b) MAPI-composite during cooling and heating in the dark.

results (see Section 3.3), we observe a trap distribution. Furthermore, Duijnstee et al. [23] have recently reported that the classical (steady state) SCLC method can lead to a wrong estimation of the charge traps density because of the ionic conductivity. To overcome these issues, in the present paper, we study charge traps density and distribution by TSC, which directly allows the investigation of defect states within the bandgap without any external applied bias, thus reducing any ionic drift.

We also measured the electron mobility in electron-only devices with the following layout: ITO/PCBM/Perovskite/PCBM/Ag, as shown in Fig. 3b. We saw from Fig. 4c, d that the current–voltage curves are quite similar for electrons, which implies a similar charge transport scenario for electrons in the MAPI and in the MAPI-composite. The average electron mobility was found to be $(1.2 \pm 0.2) \times 10^{-3}$ cm^2/Vs for the MAPI and $(2 \pm 1) \times 10^{-3}$ cm^2/Vs for the MAPI-composite. Also in this case, mobility values are similar between the MAPI and the composite samples. Furthermore, electron mobility values are similar to the hole ones, suggesting an ambipolar charge transport for both materials.

We can conclude that as we move from a neat to a composite perovskite active layer, better device stability (longer lifetime) is not gained at the expense of charge mobility, which is further confirmed by similar device performances.

3.3. Characterization of PSCs by TSC measurements

We investigate the role of the polymer upon traps formation by applying the TSC method to a working solar cell [24–27]. TSC measurements allow a direct observation of charge traps density and distribution within the bandgap in the absence of any external bias. Thus, ideally, without involving any additional ionic drift.

The MAPbI$_3$ crystal is known to have a phase transition between orthorhombic and tetragonal structures at 162 K [28,29], thus we first experimentally check the phase transition for both the neat and composite perovskite films by cooling down to 77 K and then warming up to 300 K our devices. Fig. 5 shows the TSC cooling and heating scans performed in the dark, i.e., without any traps filling, which allowed us to safely attribute the peaks to the phase transitions. It has been reported by Baumann and co-workers [25] that dark TSC profiles are polarization currents due to the reversible polarization (depolarization) of the perovskite films during the phase transition from tetragonal to orthorhombic (and vice versa). It is worth noting that our transition peak values are in perfect agreement with the already reported results on MAPI, where a shift of the heating peak between 145 K and 160 K has been observed that

was attributed to different scan rates or sample-to-sample variation due to film processing conditions and sample grains [27,30].

Independently from the absolute value of the MAPI peaks, the MAPI-composite peaks are shifted to higher temperatures likely because of an increased density of defects. According to Dobrovolsky et al. [31], a transition from the tetragonal to orthorhombic phase indeed occurs at higher temperatures when the material is characterized by domains with larger defect concentration.

Another peculiar characteristic of the MAPI-composite heating scan is the presence of both negative and positive peaks. This means there are contributions from opposite polarization directions that are present within the composite film. It has already been reported that the positive peak contribution in the MAPI perovskite is mainly due to the polarization of the cationic species in the direction perpendicular to the (110) plane [27]. Thus, the additional negative peak seen in our MAPI-composite may be due to a polarization coming from other crystal planes where the cations align in the opposite direction. Indeed, our MAPI thin film has an XRD profile characterized by a main (110) crystallographic orientation (see Fig. S2). Conversely, the MAPI-composite shows a crystallographic orientation characterized by peaks with similar intensities.

Next, we limit the temperature range of our investigation to 160–300 K, which means that we remain bound to the tetragonal phase during the entire measurement. This phase is relevant to working PSCs, and also ensures that detected traps are an intrinsic characteristic of the tetragonal phase and not a residual effect from the phase transition. The current resulting from the released carriers as a function of the temperature forms the TSC curves in Fig. 6. The same device structure was used for both materials, and thus the current values can be compared between the two devices. First, the shape of the TSC spectrum indicates a trap distribution instead of a discrete trap level. This is consistent with our SCLC measurements where a gradual rise in the current was seen in the so called TFL regime instead of a steep increase that is typical of a single trap level. By applying Eq. (2) to the TSC scan, we calculate the activation energy of the most prominent traps by

$$E_t = k_B T_{max} ln \left(\frac{T_{max}^4}{\beta} \right) \tag{2}$$

where k_B is the Boltzmann's constant, T_{max} is the temperature at the TSC peak, and β is the heating rate (5 K/min) used in the TSC measurements. The peaks $T_{max, \text{ MAPI}} = 184$ K and $T_{max,\text{MAPI-composite}} = 190$ K correspond to trap depths of 369 meV ($E_{T,\text{MAPI}}$) and 384 meV ($E_{T,\text{MAPI-composite}}$), respectively. We can also say that there
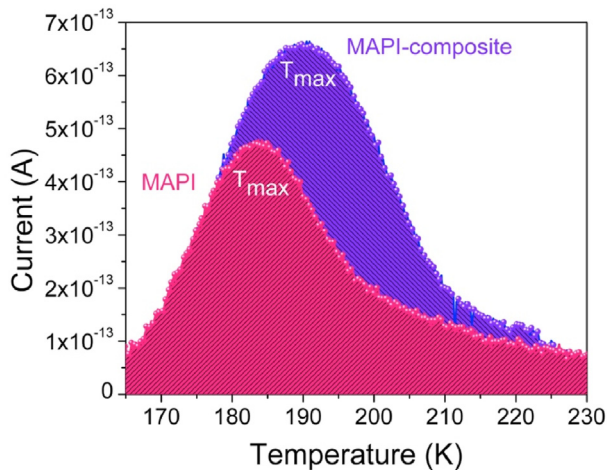
Fig. 6. TSC signals for both the MAPI (red curve) and MAPI-composite (blue curve). Both scans have been performed by heating the samples at a scan rate of 5 K/min after optically filling the traps at 160 K.

is a good similarity between the dominant trap states in both samples. A lower limit of the trap density N_t was obtained by integrating the TSC spectrum over time according to Eq. (3) [32]:

$$N_T \geq \frac{1}{ALe\beta} \int_{T_i}^{T_f} I(T) \mathrm{d}T \qquad (3)$$

where $I(T)$ is the TSC current signal, T_i and T_f are, respectively, the initial and final temperature scan, the integral $\int_{T_i}^{T_f} I(T)\mathrm{d}T$ is the area under the TSC peak, which is equal to the number of charges (in this case, holes and electrons) released from the sample during the heating process, e is the electronic charge, A is the active device area, and L is the layer thickness.

For pristine MAPI films, we found a trap concentration of 6×10^{14} cm^{-3}, which is in very good agreement with the one already reported by TSC measurements for MAPI films [25]. Furthermore, in MAPI-composites, we measured a concentration of 10×10^{14} cm^{-3} defects. This difference well explains the observed higher temperature of its phase transition. The larger concentration of defects in the MAPI-composite than that of MAPI could be possibly attributed to its polycrystalline heterogeneity, which is clearly visible in Fig. S3. The MAPI-composite SEM image reveals

the presence of well-defined polycrystalline domains whose boundaries may be the source of the larger traps' density seen in our TSC signal. This is a consequence of the polymer-assisted growth of our perovskite-composite film, which, on the one hand, allows a simpler deposition method compared to the standard ones. However, on the other, it does not permit fine control over film formation. Noticeably, our SCLC measurements demonstrated that the increased defect density in the MAPI-composite does not affect the charge carrier mobility. This could be explained by the material's well-known tolerance to defects [33—36].

3.4. Impedance spectroscopy characterization

Perovskite semiconductors are characterized by a mixed ionic and electronic charge transport mechanism. Thus, to gain insight into the possible influence of the polymer into ion migration, we perform impedance spectroscopy measurements in a temperature range of 250—300 K. Fig. S7 shows the Nyquist (Z'-Z") plots of impedance spectra for both studied configurations. The Nyquist diagrams for both samples are characterized by a complete and well-defined high-frequency arc and a second low-frequency arc whose definition depends on temperature range. The corresponding Bode plots in Fig. 7 display two peaks: one in the high frequency region and the other in the low frequency region. Analysis of the spectra reveals the existence of two kinetic processes with different time constants at high and low frequencies [37,38]. It is worth noting that the high frequency signal is independent to temperature variation. In contrary, the low-frequency signal varies accordingly and results in a shift towards higher frequencies when the sample is heated. This finding suggests that in the low frequency region of the spectra, we probed processes such as ionic migrations and/or chemical reactions that are thermally activated, whereas the high frequencies regime is usually attributed to pure electronic processes.

In order to estimate the activation energy for ion migration, Arrhenius plots were elaborated from the low frequency data extracted from Fig. 7. By fitting the impedance spectra at different temperatures with the equivalent circuit shown in Fig. S6 the characteristic time constant of the low frequency component (τ_{LF}) was calculated. The activation energy (E_a) is related to τ_{LF} and to the temperature by the following equation:

$$\frac{1}{\tau_{LF}} = Ae^{-\frac{E_a}{k_B T}} + C \qquad (4)$$

where A is the Arrhenius prefactor, k_B is the Boltzmann constant, T is the temperature, and C is a constant. The variation of the low
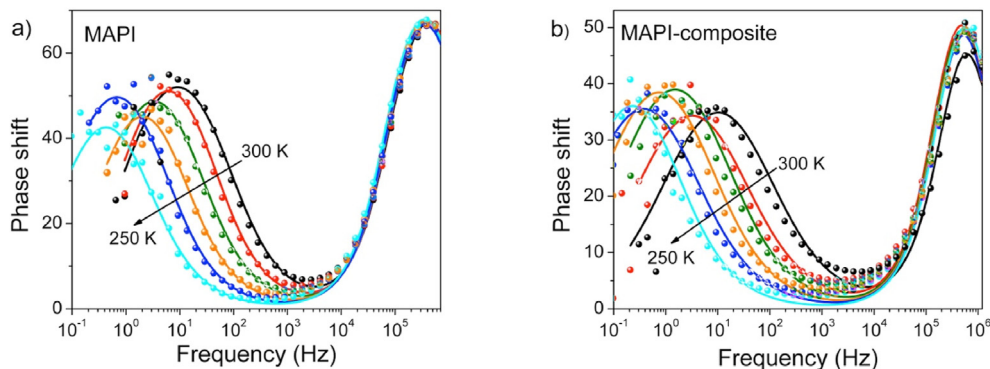

Fig. 7. Bode plots of impedance spectra obtained under 1 sun illumination and zero bias for (a) MAPI and (b) MAPI-composite-based devices. Measurements were performed in a temperature range of 250—300 K at steps of 10 K. Solid lines represent the fit to the experimental data.
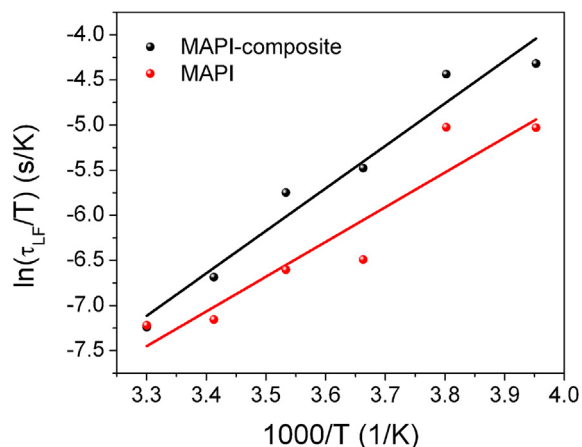
Fig. 8. Arrhenius-like plot $\ln(\tau_{LF}/T)$ versus 1000/T for MAPI and MAPI-composite. The circles are the experimental data and the solid line is the least-squares straight-line fit.

frequency time constant $(\ln(\tau_{LF}/T))$ with the inverse of the absolute temperature (1000/T) for MAPI and MAPI-composite based devices is shown in Fig. 8 where the circles are the experimental data and the solid lines are the least-squares straight-line fit.

We derived the activation energies from the slopes of the linear fit to the experimental data plotted in Fig. 8, which was about 40 and 31 kJ/mol for MAPI-composite and MAPI, respectively, with the latter one in agreement with previous literature [38—40]. It looks like the MAPI-composite is characterized by a slightly larger ionic activation energy that translates into a lower ionic conductivity that positively impacts the device stability [3]. Further investigation is ongoing in order to understand the influence of polymers on the ionic activation energy. This important result suggests additional advantages of the composite approach beyond easy processability.

4. Conclusion

In conclusion, we studied the electronic transport, trapping phenomena, phase transition, and ionic activation energy of pristine and MAPI-starch perovskite films. Our results revealed how the presence of the biopolymer impacts charge traps and ion mobility within the perovskite active layer. We observed that the MAPI-composite still retains its ambipolar charge transport nature and the same mobility values of the MAPI perovskite. This means that as we move from a neat to a composite perovskite active layer, the benefits like improved device stability, mechanical flexibility, and simpler processing are not at the expense of charge transport. Furthermore, the composite showed a lower ionic conductivity that nicely explains the higher stability with respect to the bare perovskite. These results provide a powerful guideline for the design of novel and better performing perovskite-polymer composites that anticipate the large-scale production of efficient and stable PSCs.

Declaration of competing interest

The authors declare that they have no known competing financial interests or personal relationships that could have appeared to influence the work reported in this paper.

Acknowledgments

Appendix A. Supplementary data

Supplementary data to this article can be found online at https://doi.org/10.1016/j.jsamd.2021.07.006.

References

[1] NREL efficiency, www.nrel.gov/pv/cell-efficiency.html.
[2] D. Li, D. Zhang, K. Lim, Y. Hu, Y. Rong, A. Mei, N. Park, H. Han, A review on scaling up perovskite solar cells, Adv. Funct. Mater. 31 (2021) 2008621, https://doi.org/10.1002/adfm.202008621.
[3] A. Giuri, S. Masi, A. Listorti, G. Gigli, S. Colella, C. Esposito Corcione, A. Rizzo, Polymeric rheology modifier allows single-step coating of perovskite ink for highly efficient and stable solar cells, Nanomater. Energy 54 (2018) 400—408, https://doi.org/10.1016/j.nanoen.2018.10.039.
[4] T.H. Han, J.W. Lee, C. Choi, S. Tan, C. Lee, Y. Zhao, Z. Dai, N. De Marco, S.J. Lee, S.H. Bae, Y. Yuan, H.M. Lee, Y. Huang, Y. Yang, Perovskite-polymer composite cross-linker approach for highly-stable and efficient perovskite solar cells, Nat. Commun. 10 (2019) 1—10, https://doi.org/10.1038/s41467-019-08455-z.
[5] A. Fakharuddin, M. Seybold, A. Agresti, S. Pescetelli, F. Matteocci, M.I. Haider, S.T. Birkhold, H. Hu, R. Giridharagopal, M. Sultan, I. Mora-Seró, A. Di Carlo, L. Schmidt-Mende, Perovskite-polymer blends influencing microstructures, nonradiative recombination pathways, and photovoltaic performance of perovskite solar cells, ACS Appl. Mater. Interfaces 10 (2018) 42542—42551, https://doi.org/10.1021/acsami.8b18200.
[6] Z. Safari, M.B. Zarandi, A. Giuri, F. Bisconti, S. Carallo, A. Listorti, C.E. Corcione, M.R. Nateghi, A. Rizzo, S. Colella, Optimizing the interface between hole transporting material and nanocomposite for highly efficient perovskite solar cells, Nanomaterials 9 (2019), https://doi.org/10.3390/nano9111627.
[7] A. Giuri, Z. Yuan, Y. Miao, J. Wang, F. Gao, N. Sestu, M. Saba, G. Bongiovanni, S. Colella, C. Esposito Corcione, G. Gigli, A. Listorti, A. Rizzo, Ultra-bright near-infrared perovskite light-emitting diodes with reduced efficiency roll-off, Sci. Rep. 8 (2018) 1—8, https://doi.org/10.1038/s41598-018-33729-9.
[8] S. Gambino, The impact of charge carrier relaxation, electron trapping and oxygen p-doping on the photocurrent transients of a conjugated polymer probed by the Time of Flight method, Thin Solid Films 718 (2021) 138485, https://doi.org/10.1016/j.tsf.2020.138485.
[9] P. Calado, A.M. Telford, D. Bryant, X. Li, J. Nelson, B.C. O'regan, P.R.F. Barnes, Evidence for ion migration in hybrid perovskite solar cells with minimal hysteresis, Nat. Commun. 7 (2016), https://doi.org/10.1038/ncomms13831.
[10] D. Li, H. Wu, H.C. Cheng, G. Wang, Y. Huang, X. Duan, Electronic and ionic transport dynamics in organolead halide perovskites, ACS Nano 10 (2016) 6933—6941, https://doi.org/10.1021/acsnano.6b02795.
[11] P. Lopez-Varo, J.A. Jiménez-Tejada, M. García-Rosell, S. Ravishankar, G. Garcia-Belmonte, J. Bisquert, O. Almora, Device physics of hybrid perovskite solar cells: theory and experiment, Adv. Energy Mater 8 (2018), https://doi.org/10.1002/aenm.201702772.
[12] M. Kuik, G.-J.J.A.H. Wetzelaer, H.T. Nicolai, N.I. Craciun, D.M. De Leeuw, P.W.M. Blom, 25th anniversary article: charge transport and recombination in polymer light-emitting diodes, Adv. Mater. 26 (2014) 512—531, https://doi.org/10.1002/adma.201303393.
[13] M. Sajedi Alvar, P.W.M. Blom, G.-J.A.H. Wetzelaer, Space-charge-limited electron and hole currents in hybrid organic-inorganic perovskites, Nat. Commun. 11 (2020) 4023, https://doi.org/10.1038/s41467-020-17868-0.
[14] K.C. Kao, Dielectric Phenomena in Solids, Elsevier, 2004.
[15] Y. Chen, J. Peng, D. Su, X. Chen, Z. Liang, Efficient and balanced charge transport revealed in planar perovskite solar cells, ACS Appl. Mater. Interfaces 7 (2015) 4471—4475, https://doi.org/10.1021/acsami.5b00077.
[16] J. Peng, Y. Chen, K. Zheng, T. Pullerits, Z. Liang, Insights into charge carrier dynamics in organo-metal halide perovskites: from neat films to solar cells, Chem. Soc. Rev. 46 (2017) 5714—5729, https://doi.org/10.1039/c6cs00942e.
[17] G. Zuo, Z. Li, O. Andersson, H. Abdalla, E. Wang, M. Kemerink, Molecular doping and trap filling in organic semiconductor host-guest systems, J. Phys. Chem. C 121 (2017) 7767—7775, https://doi.org/10.1021/acs.jpcc.7b01758.
[18] G. Zuo, M. Linares, T. Upreti, M. Kemerink, General rule for the energy of water-induced traps in organic semiconductors, Nat. Mater. 18 (2019) 588—593, https://doi.org/10.1038/s41563-019-0347-y.
[19] M. De Bastiani, G. Dell'Erba, M. Gandini, V. D'Innocenzo, S. Neutzner, A.R.S. Kandada, G. Grancini, M. Binda, M. Prato, J.M. Ball, M. Caironi, A. Petrozza, Ion migration and the role of preconditioning cycles in the stabilization of the J-V characteristics of inverted hybrid perovskite solar cells, Adv. Energy Mater 6 (2016) 1—9, https://doi.org/10.1002/aenm.201501453.
[20] Z. Xu, T. De Rosia, K. Weeks, Photoluminescence-voltage (PL-V) hysteresis of perovskite solar cells, J. Phys. Chem. C 121 (2017), https://doi.org/10.1021/acs.jpcc.7b06711.

[21] M. Sajedi Alvar, P.W.M. Blom, G.A.H. Wetzelaer, Device model for methyl-ammonium lead iodide perovskite with experimentally validated ion dynamics, Adv. Electron. Mater. 6 (2020) 1900935, https://doi.org/10.1002/aelm.201900935.

[22] S. Chaudhary, S.K. Gupta, C.M. Singh Negi, Enhanced performance of perovskite photodetectors fabricated by two-step spin coating approach, Mater. Sci. Semicond. Process. 109 (2020) 104916, https://doi.org/10.1016/j.mssp.2020.104916.

[23] E.A. Duijnstee, J.M. Ball, V.M. Le Corre, L.J.A. Koster, H.J. Snaith, J. Lim, Toward understanding space-charge limited current measurements on metal halide perovskites, ACS Energy Lett. 5 (2020) 376–384, https://doi.org/10.1021/acsenergylett.9b02720.

[24] C. Qin, T. Matsushima, T. Fujihara, W.J. Potscavage, C. Adachi, Degradation mechanisms of solution-processed planar perovskite solar cells: thermally stimulated current measurement for analysis of carrier traps, Adv. Mater. 28 (2016) 466–471, https://doi.org/10.1002/adma.201502610.

[25] A. Baumann, S. Väth, P. Rieder, M.C. Heiber, K. Tvingstedt, V. Dyakonov, Identification of trap states in perovskite solar cells, J. Phys. Chem. Lett. 6 (2015) 2350–2354, https://doi.org/10.1021/acs.jpclett.5b00953.

[26] G. Gordillo, C.A. Otálora, M.A. Reinoso, Trap center study in hybrid organic-inorganic perovskite using thermally stimulated current (TSC) analysis, J. Appl. Phys. 122 (2017) 75304, https://doi.org/10.1063/1.4999297.

[27] S.T. Birkhold, H. Hu, P.T. Höger, K.K. Wong, P. Rieder, A. Baumann, L. Schmidt-Mende, Mechanism and impact of cation polarization in methylammonium lead iodide, J. Phys. Chem. C 122 (2018) 12140–12147, https://doi.org/10.1021/acs.jpcc.8b00631.

[28] A. Poglitsch, D. Weber, Dynamic disorder in methylammonium-trihalogenoplumbates (II) observed by millimeter-wave spectroscopy, J. Chem. Phys. 87 (1987) 6373, https://doi.org/10.1063/1.453467.

[29] N. Onoda-Yamamuro, T. Matsuo, H. Suga, Dielectric study of CH3NH3PbX3 (X = Cl, Br, I), J. Phys. Chem. Solid. 53 (1992) 935–939, https://doi.org/10.1016/0022-3697(92)90121-S.

[30] A. Osherov, E.M. Hutter, K. Galkowski, R. Brenes, D.K. Maude, R.J. Nicholas, P. Plochocka, V. Bulović, T.J. Savenije, S.D. Stranks, The impact of phase retention on the structural and optoelectronic properties of metal halide perovskites, Adv. Mater. 28 (2016) 10757–10763, https://doi.org/10.1002/adma.201604019.

[31] A. Dobrovolsky, A. Merdasa, E.L. Unger, A. Yartsev, I.G. Scheblykin, Defect-induced local variation of crystal phase transition temperature in metal-halide perovskites, Nat. Commun. 8 (2017) 34, https://doi.org/10.1038/s41467-017-00058-w.

[32] P. Stallinga, Electrical Characterization of Organic Electronic Materials and Devices, 2009, https://doi.org/10.1002/9780470750162.

[33] A. Zakutayev, C.M. Caskey, A.N. Fioretti, D.S. Ginley, J. Vidal, V. Stevanovic, E. Tea, S. Lany, Defect tolerant semiconductors for solar energy conversion, J. Phys. Chem. Lett. 5 (2014) 1117–1125, https://doi.org/10.1021/jz5001787.

[34] J. Kim, S.-H. Lee, J.H. Lee, K.-H. Hong, The role of intrinsic defects in methylammonium lead iodide perovskite, J. Phys. Chem. Lett. 5 (2014) 1312–1317, https://doi.org/10.1021/jz500370k.

[35] H. Jin, E. Debroye, M. Keshavarz, I.G. Scheblykin, M.B.J. Roeffaers, J. Hofkens, J.A. Steele, It's a trap! on the nature of localised states and charge trapping in lead halide perovskites, Mater. Horizons 7 (2020) 397–410, https://doi.org/10.1039/c9mh00500e.

[36] R.E. Brandt, J.R. Poindexter, P. Gorai, R.C. Kurchin, R.L.Z. Hoye, L. Nienhaus, M.W.B. Wilson, J.A. Polizzotti, R. Sereika, R. Žaltauskas, L.C. Lee, J.L. Macmanus-Driscoll, M. Bawendi, V. Stevanović, T. Buonassisi, Searching for "defect-tolerant" photovoltaic materials: combined theoretical and experimental screening, Chem. Mater. 29 (2017) 4667–4674, https://doi.org/10.1021/acs.chemmater.6b05496.

[37] J.R.M. Barsoukov, Evgenij, Impedance Spectroscopy Theory, Experiment, and Applications, Second, John Wiley & Sons, 2005.

[38] L. Contreras-Bernal, S. Ramos-Terrón, A. Riquelme, P.P. Boix, J. Idígoras, I. Mora-Seró, J.A. Anta, Impedance analysis of perovskite solar cells: a case study, J. Mater. Chem. 7 (2019) 12191–12200, https://doi.org/10.1039/c9ta02808k.

[39] Y. Yuan, J. Chae, Y. Shao, Q. Wang, Z. Xiao, A. Centrone, J. Huang, Photovoltaic switching mechanism in lateral structure hybrid perovskite solar cells, Adv. Energy Mater 5 (2015) 1–7, https://doi.org/10.1002/aenm.201500615.

[40] S. Meloni, T. Moehl, W. Tress, M. Franckeviius, M. Saliba, Y.H. Lee, P. Gao, M.K. Nazeeruddin, S.M. Zakeeruddin, U. Rothlisberger, M. Graetzel, Ionic polarization-induced current-voltage hysteresis in CH3NH3PbX3 perovskite solar cells, Nat. Commun. 7 (2016), https://doi.org/10.1038/ncomms10334.